Supporting information

Asymmetric Assembling of Iron Oxide Nanocubes for Improving Magnetic Hyperthermia Performance

Dina Niculaes[1,2,*], Aidin Lak[1,*], George C. Anyfantis[1], Sergio Marras[1], Oliver Laslett[3], Sahitya K. Avugadda,[1,2] Marco Cassani,[1,2] David Serantes[4], Ondrej Hovorka[3], Roy Chantrell[5], and Teresa Pellegrino[1]

[1] Istituto Italiano di Tecnologia, Via Morego 30, 16163 Genova, Italy

[2] Dipartimento di Chimica e Chimica Industriale, Università di Genova, Via Dodecaneso 31, 16146 Genova, Italy

[3] Engineering and the Environment, University of Southampton, Southampton, SO16 7QF, UK

[4] Applied Physics Department and Instituto de Investigacións Tecnolóxicas, Universidade de Santiago de Compostela, 15782, Spain

[5] Department of Physics, University of York, York, YO10 5DDUnited Kingdom

* These authors contributed equally to this work.

Email: teresa.pellegrino@iit.it

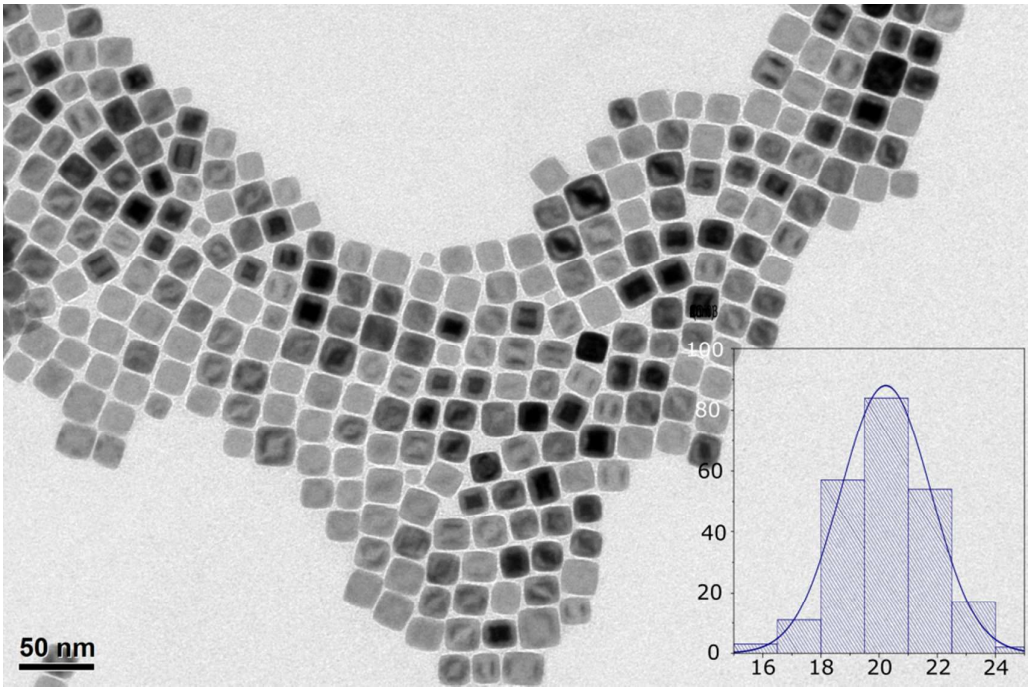

Figure S1: Representative TEM micrograph of freshly prepared as-synthesized core-shell iron oxide nanocubes (sample A) dispersed in chloroform and used for the cluster formation (inset: size histogram, a = 20.2 ± 1.5 nm).

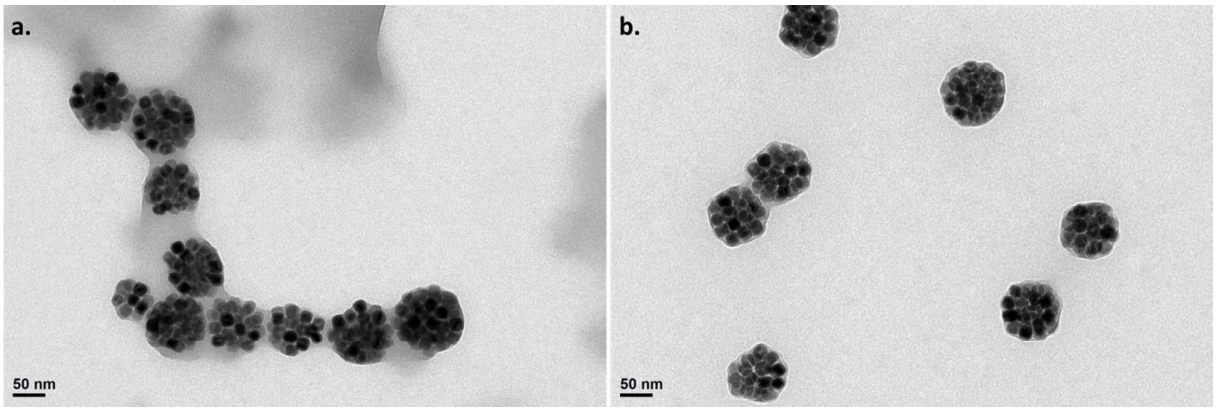

Figure S2: Impact of $CHCl_3$ addition as the last step in the cluster formation process. TEM micrographs of clusters made of 19 nm core-shell IONCs in water (a) before $CHCl_3$ addition, and (b) after $CHCl_3$ addition. Before the addition of $CHCl_3$ a polymer layer was observed on the TEM grid. After $CHCl_3$ addition the excess of polymer was removed and no longer present in the aqueous phase.

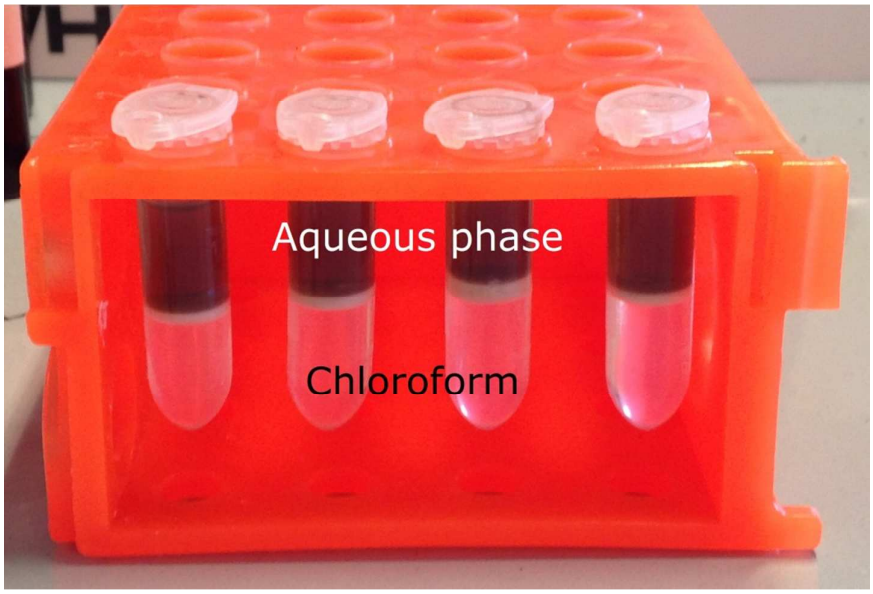

Figure S3: Addition of chloroform as the last step in cluster formation, in order to remove the excess of polymer. Both aqueous and organic phases are clear. The excess of polymer is seen as a white layer at the interface between the two phases.

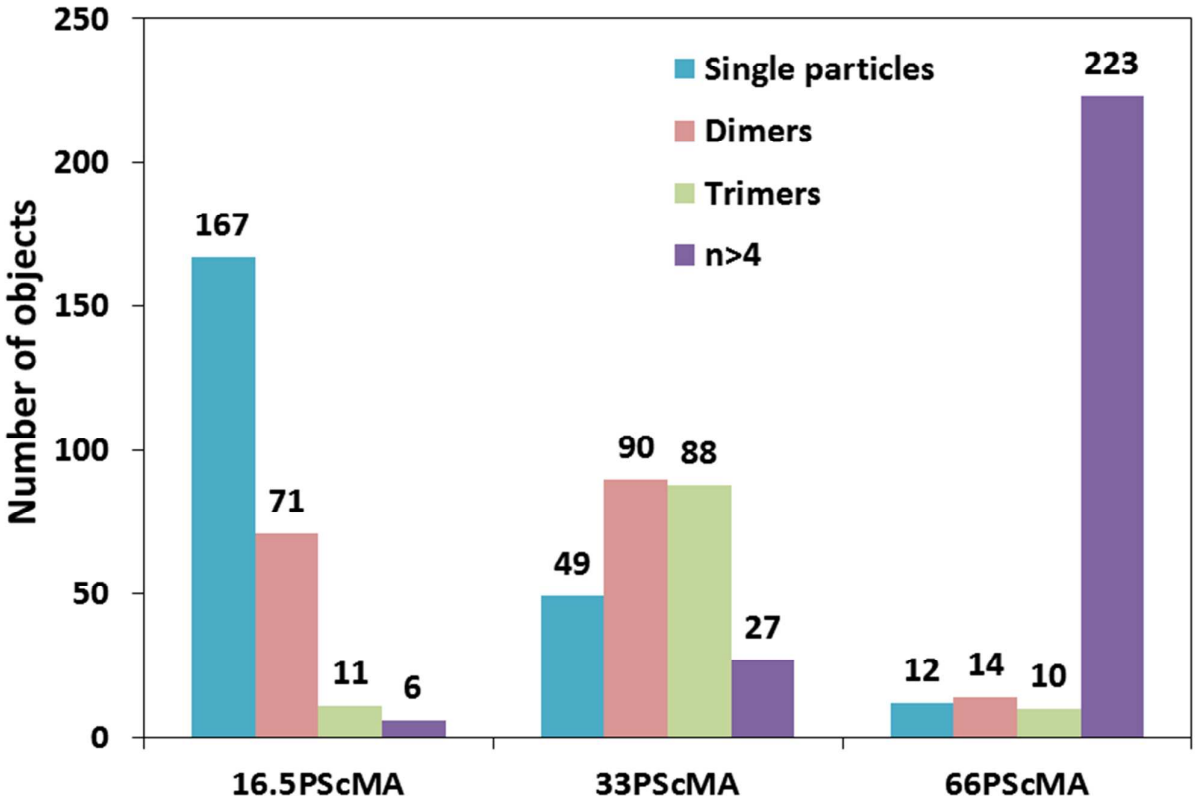

Figure S4: Statistical distributions, by number of objects, for samples 16.5PS*c*MA, 33PS*c*MA and 66PS*c*MA

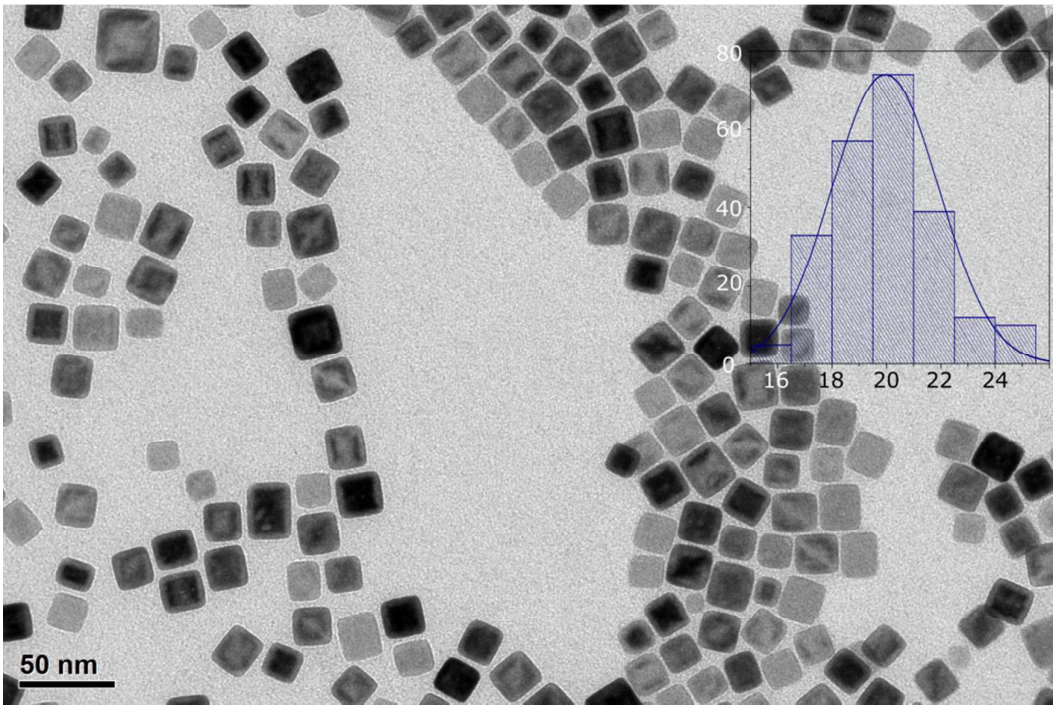

Figure S5: Representative TEM micrograph of sample B of freshly prepared as-synthesized core-shell iron oxide nanocubes dispersed in chloroform (inset: size histogram, a = 20 ± 2 nm).

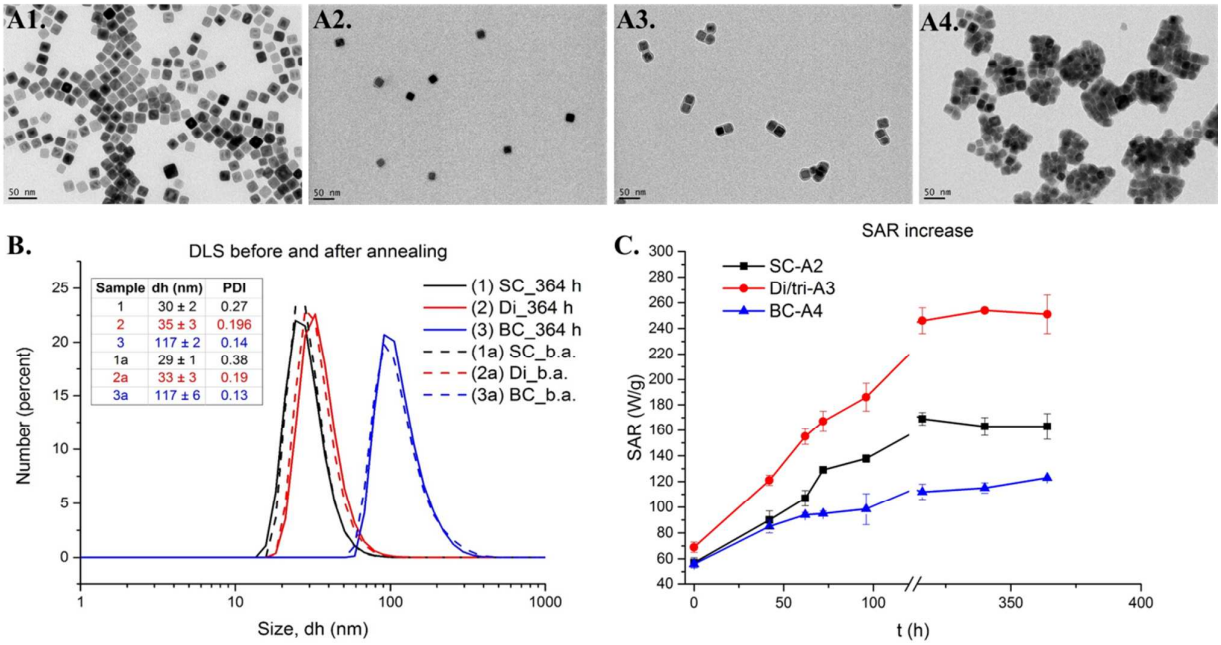

Figure S6. Implementation of the clustering procedure when using another type of core-shell FeO/Fe_xO_y nanocubes prepared with a different method by adopting the protocol reported by Wetterskog et al.[1] and Begin Colin *et al.*[2] (A) Representative TEM micrographs of clusters in water (18 nm IONC): (A1) initial nanoparticles in $CHCl_3$, (A2) single cubes (SC) at 12 polymer chains/nm^2, (A3) Dimer (Di) and trimers (tri) at 18 polymer chains/nm^2, (A4) bigger clusters (BC) at 35.5 polymer chains/nm^2. (B) Mean hydrodynamic sizes

before (dash lines) and after (solid line) the annealing process for the three samples. (C) SAR values, with standard deviation, plotted at different annealing times for individual IONCs—black line, dimers and trimers—red line, and clusters with n ≥ 4—blue line.

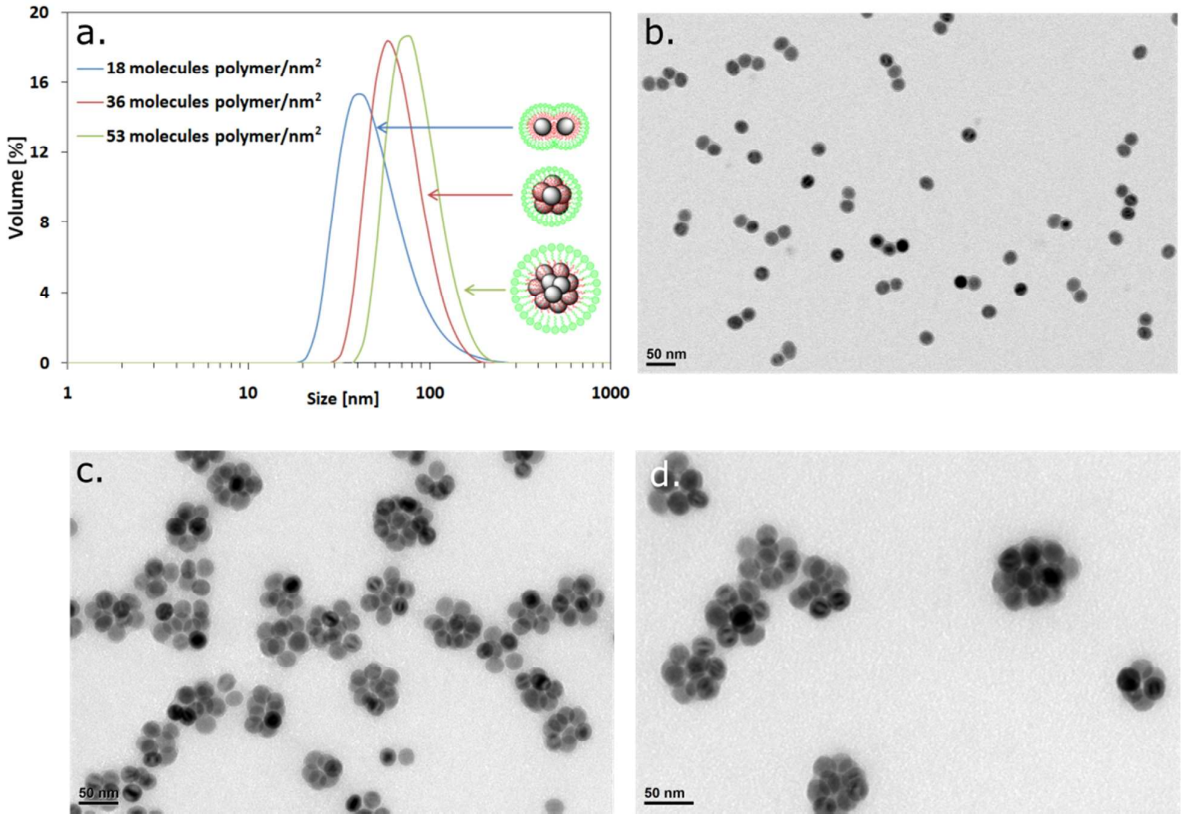

Figure S7. Implementation of the clustering procedure when using 22 nm spherical IONPs prepared by a seede growth method[3]. (a) Volume distribution of hydrodynamic size of soft colloidal clusters measured in water. The d_H was estimated between 52 and 86 nm. No aggregation of clusters was detected as PDI values were between 0.06 and 0.19. (b-d) Representative TEM micrographs of IONPs@PS*c*MA in water, shortly after they have been prepared at a ratio of (b) 18, (c) 36, and (d) 53 polymer chains/nm^2 of particle surface, respectively.

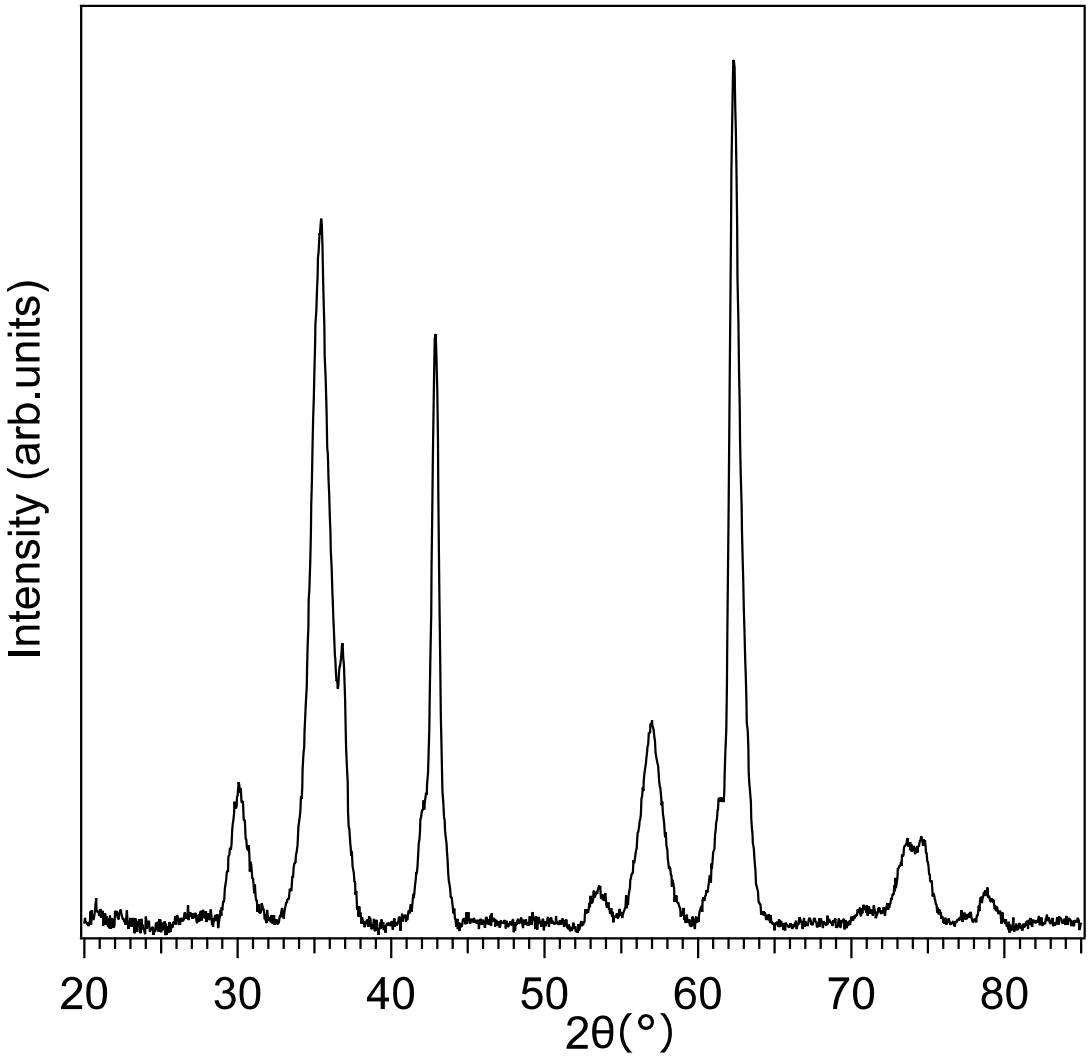

Figure S8: XRD pattern of one-year aged nanocubes (sample A) in chloroform that were used one year prior to form 16.5PS*c*MA, 33PS*c*MA, and 66PS*c*MA samples. The broad reflections at around 42° and 62° are attributed to the FeO phase. Quantitative phase analysis showed that the fraction of FeO in these particles is around 10-15 *wt%*.

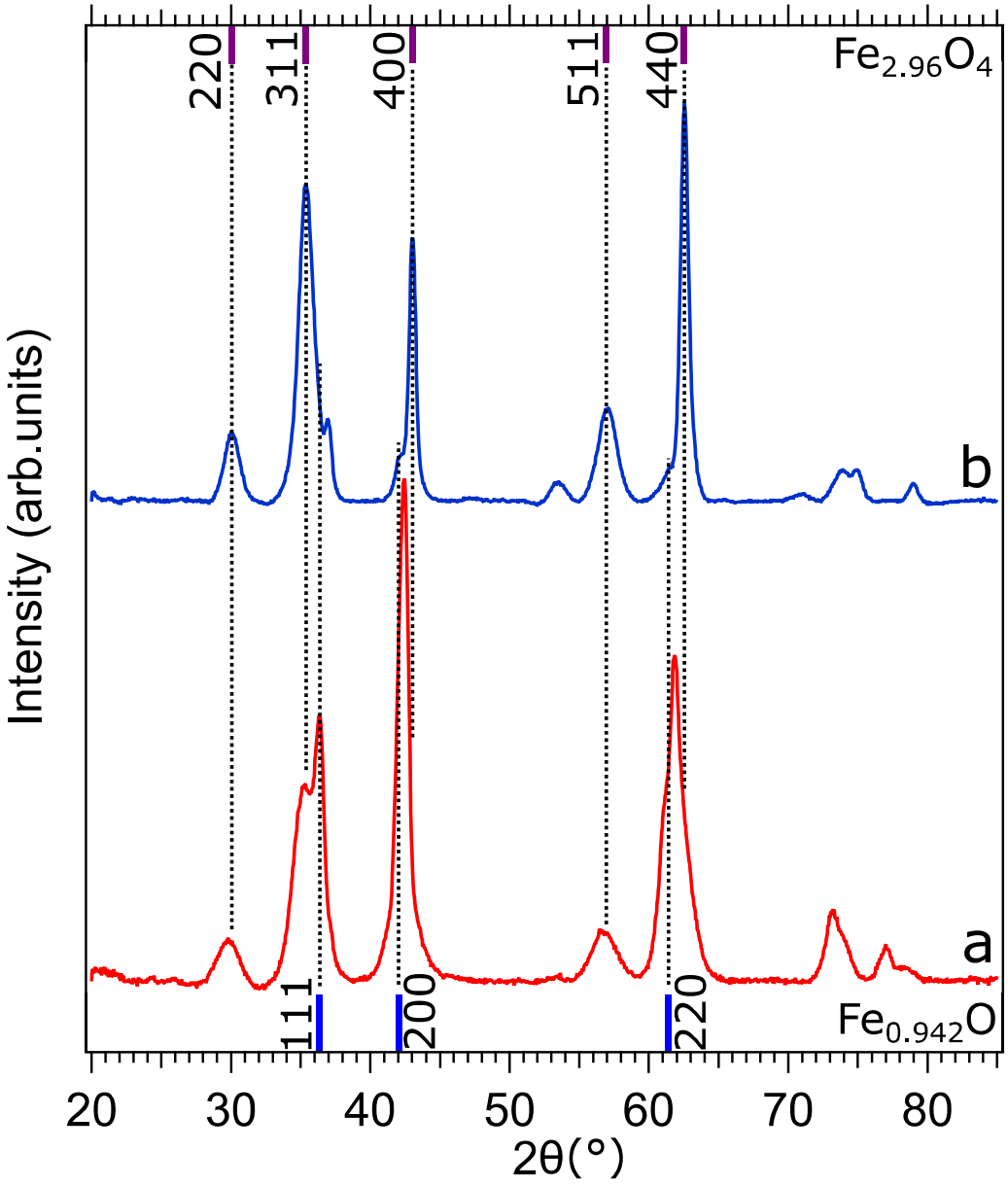

Figure S9: XRD pattern of 20 ± 2 nm core-shell iron oxide nanocubes (Fig. S5) (a) before (thus freshly prepared) and (b) after 52 h annealing in oven at 80 °C.

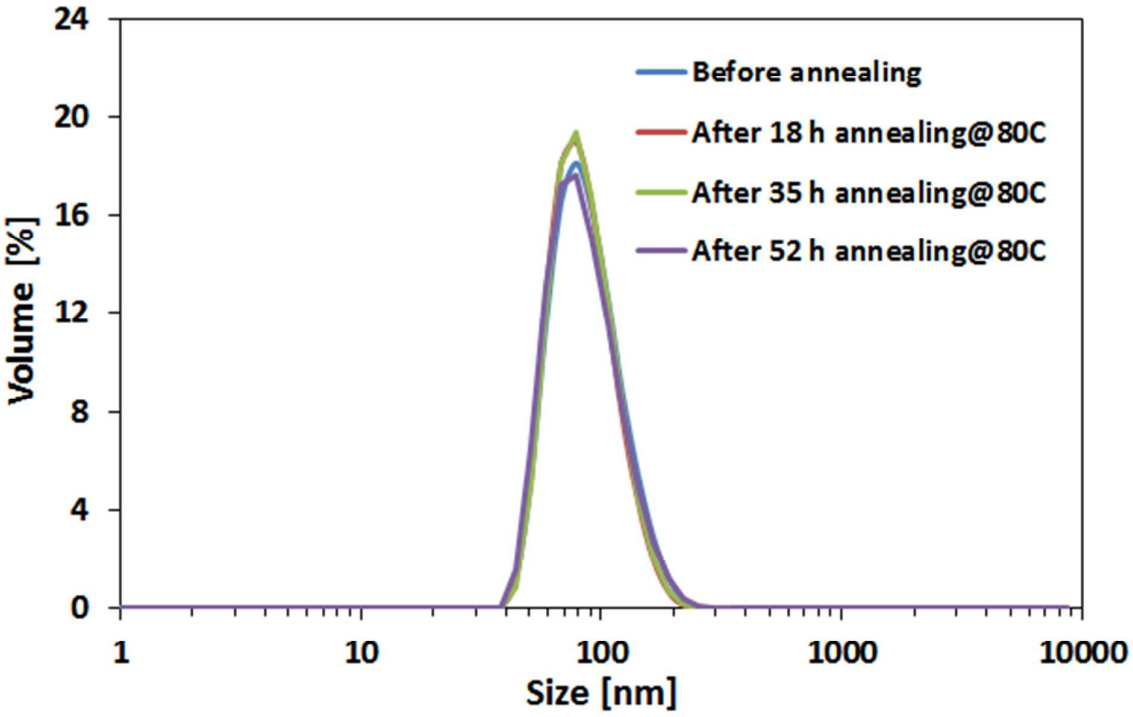

Figure S10: Stability of the mean hydrodynamic diameter during annealing experiments. Volume distribution of hydrodynamic size d_H of centrosymmetric soft colloidal nanoclusters before annealing (blue line), after 18 hours (red line), 35 hours (green line), and 52 hours (violet line) of annealing at 80°C. The sample was stable under annealing at 80 °C, as no aggregation occurred. Z-average before annealing: 98.1 ± 0.6 nm (PDI 0.07), after 52 hours of annealing: 96.5 ± 0.2 (PDI 0.08).

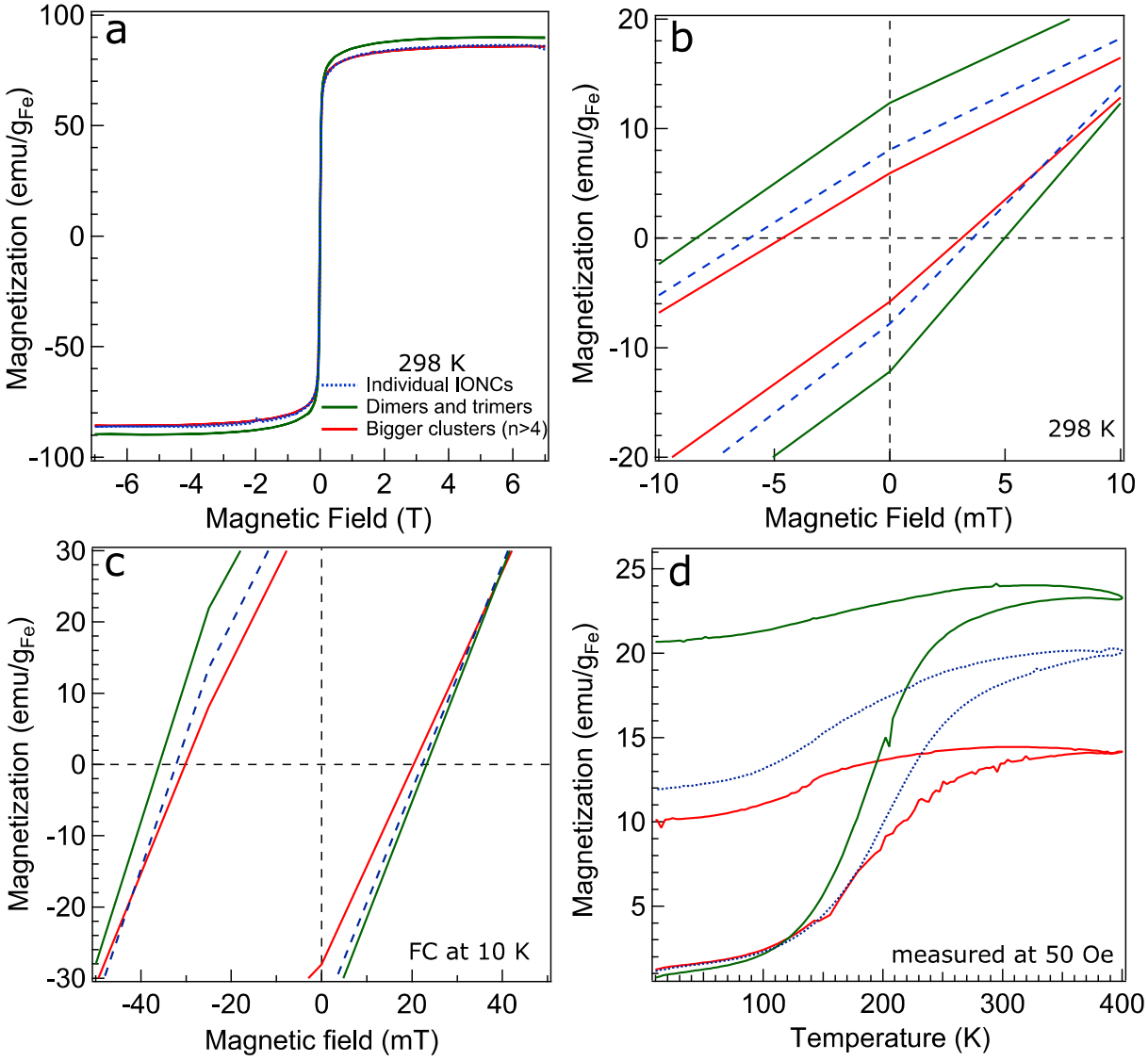

Figure S11: Magnetization hysteresis loops for clusters obtained from sample B after 52 hours annealing time at 80°C, measured at room temperature (a) and (b) and after cooling to 10 K in 5 T magnetic fields (c), and temperature dependent zero-field-cooled and field-cooled magnetization measurements performed on aqueous suspension of nanoclusters solidified in gypsum matrix recorded at 50 Oe magnetic fields (d): individual IONCs—dashed blue line, dimers and trimers—green line, and clusters with n ≥ 4—red line.

Table S1. Comparisons of synthesis parameter and properties of sample A and sample B

	Sample A	**Sample B**
Synthesis		
- *sodium oleate* [g]	0.939	0.939
- *oleic acid* [g]	1.6	2.6
- *1-octadecene* [mL]	5	3
Size [nm]	20.2 ± 1.5	20± 2
Surfactant		
- *weight loss before washing* [*wt%*]	1st: 26.4 2nd: 31.2	1st: 11.5 2nd: 68.1
- *weight loss after washing*	-	1st: 11.5 2nd: 43.3
SAR [W/g_{Fe}]		
- *individual particles*	213 ± 9	162 ± 7*
- *dimers and trimers*	253 ± 10	246 ± 8*
- *bigger clusters*	184 ± 8	150 ± 3*

*: SAR values after thermal annealing in the oven @80 °C for 52 hours.

Modelling of magnetization behavior of particle clusters

Kinetic Monte-Carlo model as described in the methodology section in the main text is applied to study the magnetization behavior of the experimentally relevant cluster structures. Except for data in Figure S16, all simulation results reported in the ESI have been generated assuming constant $M_s = 450$ emu/cm^3 consistent with the bulk value for Fe_3O_4. Figure S12 shows examples of the simulated cluster structures. Figures S13-S14 show major hysteresis loops corresponding to the cluster structures for two extreme cases of the uniaxial anisotropy value. In Fig. S13 dipolar behavior dominates the anisotropy field (low *K*), which has profound effects on the shape of the hysteresis loop for the different cluster types. In S12 dipolar interactions are negligible (high *K*), and the variation of the major hysteresis loops between the different cluster structures is not so significant. This suggests, that to qualitatively model the variations in SAR of experimental results in Figs. 5 and 7, it is required to consider dominating dipolar interactions, *i.e.* setting low K in the modelling. The reason we simulated major loops in Figs. S13-S14 and not the low applied field loops relevant experimentally is that at low fields the minor hysteresis loops become noisier, which requires data averaging and is not suitable for visualizations. In Fig. S13-14 we wanted to highlight the differences in the behavior induced by the anisotropy and dipolar effects for which showing the major hysteresis loops is sufficient.

Fig. S15 shows the variation of the SAR for different anisotropy values *K* for all relevant cluster types, assuming the applied field amplitude and frequency consistent with our experiments. Figs. S15(D) and (E) qualitatively recover the experimental trends which, given that the simulated data corresponds to fixed

$M_S = 450$ kA/m suggests that the variation of the M_S in experimental clusters is not the primary factor behind the trend of variation of SAR observed in Figs. 5 and 7, but rather that these differences are due to the dipolar effect induced by the varying geometry of particle arrangements in the different cluster types.

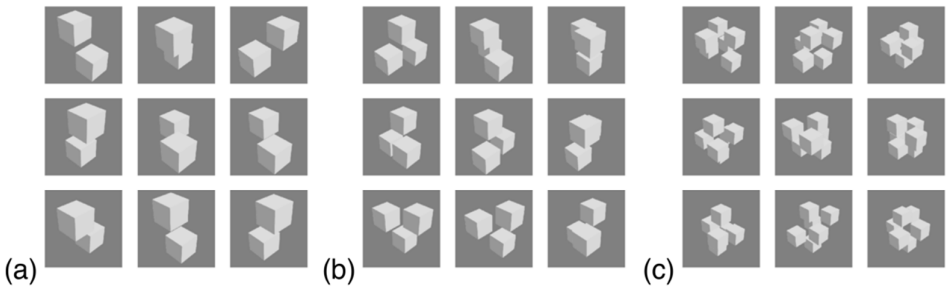

Figure S12: Snapshots showing examples of randomized particle structures in the simulated particle ensembles (a) 2-particle clusters (dimers), (b) 3-particle clusters (trimers), and (c) 6-particle clusters. The total number of nanocubes in each ensemble is 3000 and there are 1500 dimers, 1000 trimers, and 500 6-particle clusters in each simulated ensemble. The nanocube size edge used in simulations is 20 nm and cube-cube centre-to-centre distance inside clusters is set to 23 nm.

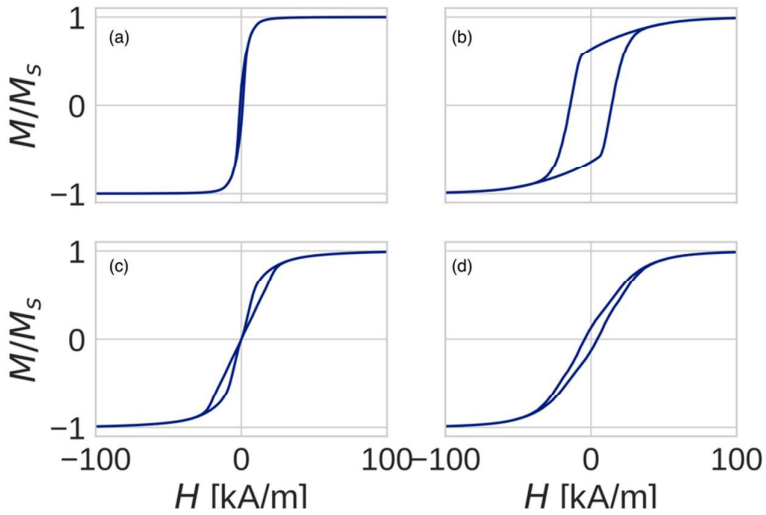

Figure S13: Examples of dynamic major hysteresis loops calculated at the applied field frequency of the experiment $f = 300$ kHz and field amplitude $H_0 = 140$ kA/m ($H_0 = 180$ mT) sufficient to saturate particles, for a system of (a) 3000 non-interacting particles, (b) 1500 dimers, (c) 1000 trimers, and (d) 500 6-particle clusters. The uniaxial anisotropy value used in calculations was $K = 3 \times 10^4$ erg/cm^3. All simulations assume saturation magnetization of $M_S = 450$ kA/m. Given the low value of K, dipolar

interactions are expected to dominate the behavior and the loop shape changes significantly between the different cluster types.

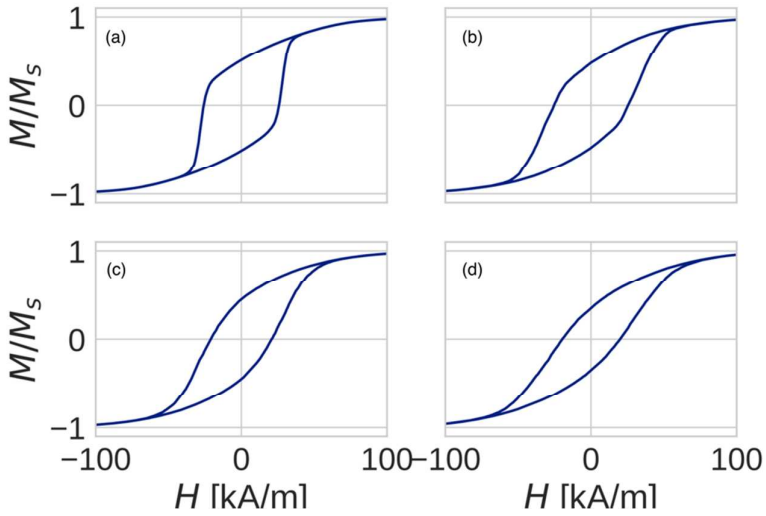

Figure S14: Examples of dynamic major hysteresis loops calculated at the applied field frequency of the experiment $f = 300$ kHz and field amplitude $H_0 = 140$ kA/m ($H_0 = 180$ mT) sufficient to saturate particles, for a system of (a) 3000 non-interacting particles, (b) 1500 dimers, (c) 1000 trimers, and (d) 500 6-particle clusters. The uniaxial anisotropy value used in calculations was $K = 1 \times 10^5$ erg/cm^3. All simulations assume saturation magnetization of $M_S = 450$ kA/m. At this value of K, the anisotropy field dominates the dipolar interactions and the hysteresis loops are influenced by dipolar interactions only mildly.

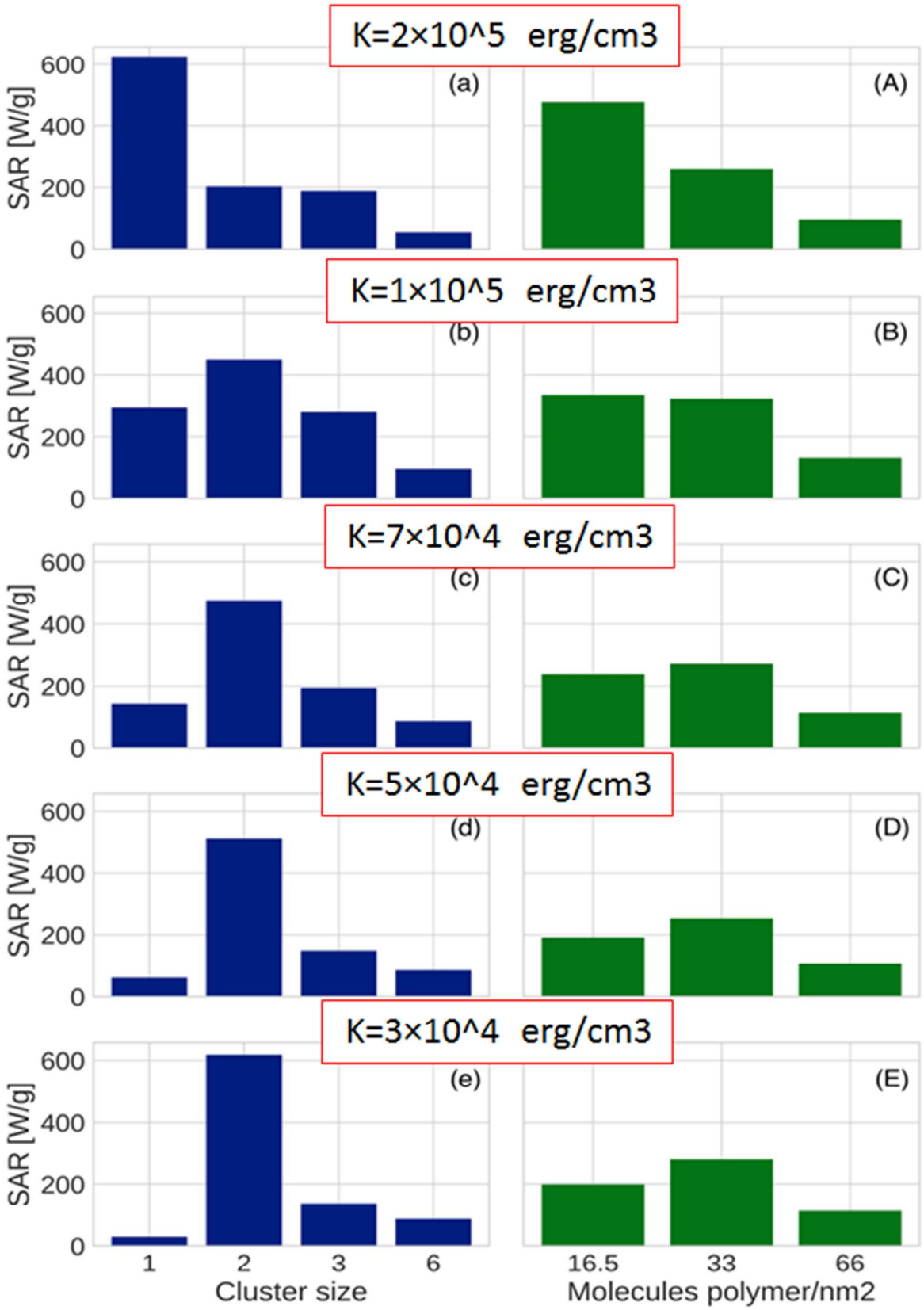
K=2×10^5 erg/cm3
K=1×10^5 erg/cm3
K=7×10^4 erg/cm3
K=5×10^4 erg/cm3
K=3×10^4 erg/cm3
SAR [W/g]
0
200
400
600
(a)
(b)
(c)
(d)
(e)
(A)
(B)
(C)
(D)
(E)
1
2
3
6
Cluster size
16.5
33
66
Molecules polymer/nm2

Figure S15: Effect of the magnitude of uniaxial anisotropy constant K on SAR. Subfigures correspond to SAR simulations obtained by decreasing order of K values (a-A) $K = 2 \times 10^5$ erg/cm^3, (b-B) $K = 1 \times 10^5$ erg/cm^3, (c-C) $K = 7 \times 10^4$ erg/cm^3, (d-D) $K = 5 \times 10^4$ erg/cm^3, and (e-E) $K = 3 \times 10^4$ erg/cm^3. All simulations assumed saturation magnetization of $M_s = 450$ kA/m, applied field magnitude $H_0 = 23.8$ kA/m and frequency $f = 300$ kHz. Left column (a-e) corresponds to SAR calculations for individual ensembles of non-interacting particles (1), 2-particle clusters (2), 3-particle clusters (3), and 6-particle clusters (6). The right column (A-E) shows the data from (a-e) combined to reflected mixed population of clusters according to statistical data as reported in Fig. 3 in the main text. The data in the left column show that as the anisotropy value K decreases the SAR in the non-interacting case (1) decreases, which can be attributed to the reduction of the particle energy barriers. The trend is opposite for 2-cube clusters (2), which is due to the increased contribution from the dipolar interactions relative to the decreasing energy barrier. For the 3-cube (3) and higher order clusters (6) there is an increased tendency to form magnetic flux closure, which reduces their overall interaction with the external magnetic field and leads to the observation of decreased values of SAR. The right column Figures (D) and (E) closely resemble the trends seen in the main figures 5 and 7. Given that the simulated data corresponds to fixed $M_s = 450$ kA/m, these results suggest that the variation of the M_s in experimental clusters is not the primary reasons behind the trend of variation of SAR observed in Figs. 5 and 7, but rather that these differences are due to the varying geometry of the particle arrangements in the different cluster types.

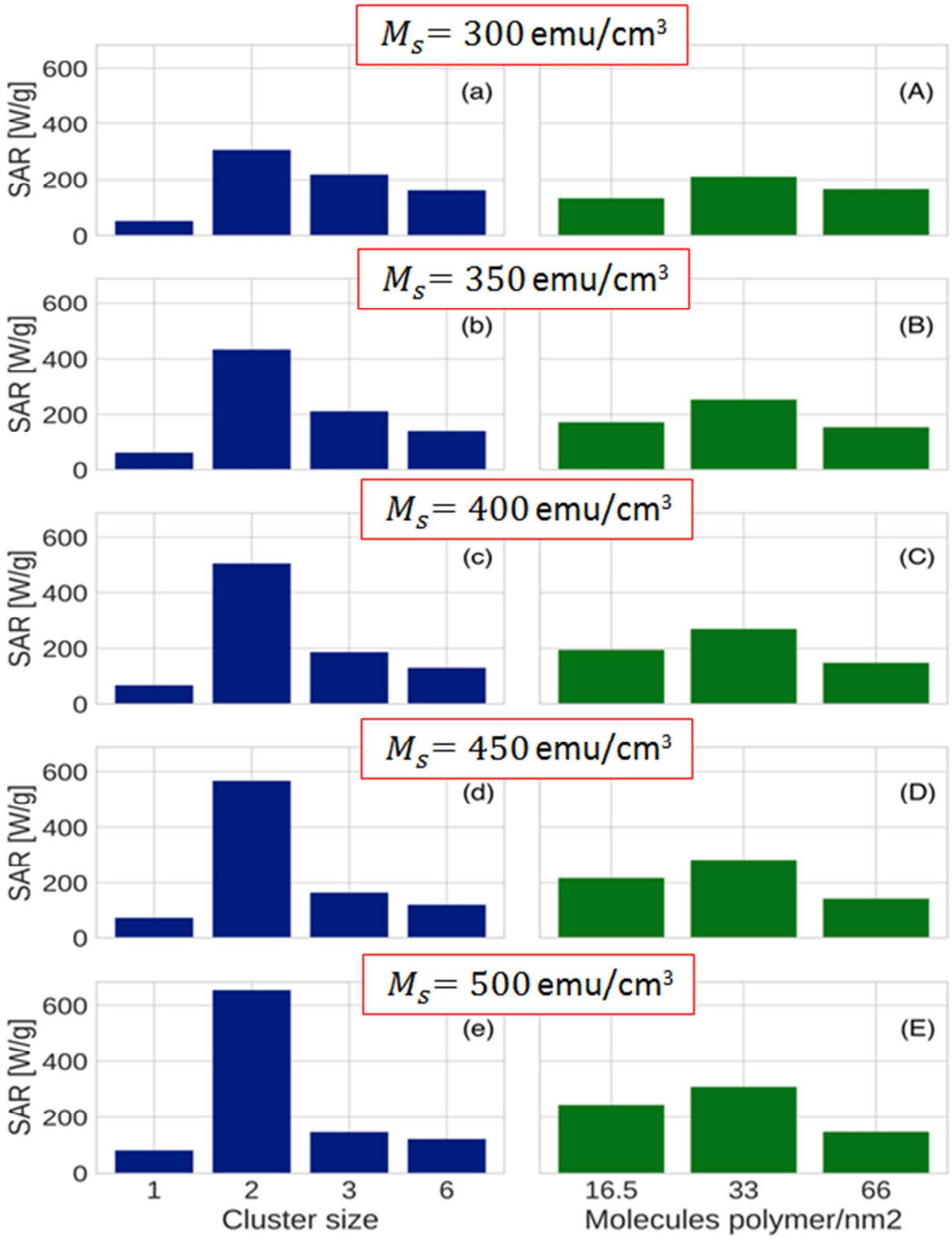

Figure S16: Effect of the magnitude of magnetization of saturation, M_s on SAR. Subfigures correspond to SAR simulations obtained for (a-A) $M_s = 300$ emu/cm^3, (b-B) $M_s = 350$ emu/cm^3, (c-C) $M_s = 400$ emu/cm^3, (d-D) $M_s = 450$ emu/cm^3, and (e-E) $M_s = 500$ emu/cm^3. All simulations assumed the anisotropy value $K = 5 \times 10^4$ erg/cm^3, applied field magnitude $H_0 = 23.8$ kA/m and frequency $f = 300$

kHz. Left column (a-e) corresponds to SAR calculations for individual ensembles of non-interacting particles (1), 2-particle clusters (2), 3-particle clusters (3), and 6-particle clusters (6). The right column (A-E) shows the data from (a-e) combined to reflected mixed population of clusters according to statistical data as reported in Fig. 3 in the main text. The data in the left column show that as M_S value increases the variation of SAR in the non-interacting case (1) is only small, in agreement with the argumentation in the main text. The 2-cube clusters (2) show increasing SAR with increasing M_S, which is due to the increased constructive contribution from the dipolar interactions. For the 3-cube (3) and higher order clusters (6) SAR decreases with increasing value of M_S, which can be attributed to the formation of the magnetic flux closure domains. The overall trends of SAR for the different cluster types in columns (a-e) and (A-E) remain preserved, which suggests that the differences in SAR are due to the varying geometry of the particle arrangements in the different cluster types.

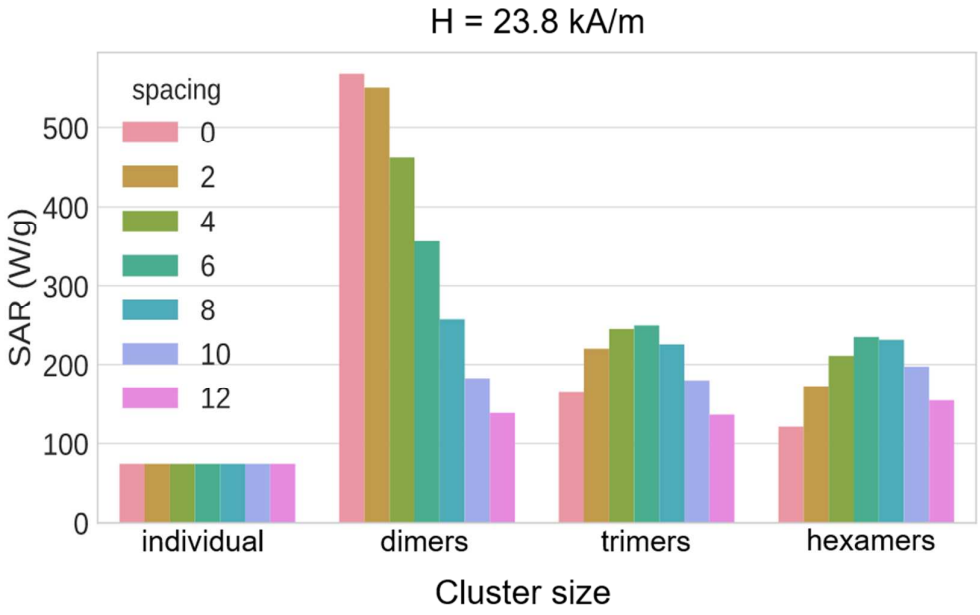

Figure S17: Dependence of SAR on the inter-particle edge-to-edge spacing for the different cluster geometries considered in the study, namely the non-interacting particles (individual), and 2-particle (dimers), 3-particle (trimers), and 6-particle (hexamers) clusters as illustrated in Fig. 5 in the main text. Increasing the inter-particle spacing (from 0 to 12 nm) decreases the strength of dipolar interaction between the particles inside the clusters. For non-interacting particles the dipolar interaction is zero and SAR is independent of inter-particle spacing. Simulations assumed $K = 5 \times 10^4$ erg/cm^3, saturation magnetization $M_S = 450$ emu/cm^3, applied field magnitude $H_0 = 23.8$ kA/m, and frequency $f = 300$ kHz.

Ensembles contained 3000 particles, *i.e.* 1500 2-particle clusters, 1000 3-particle clusters, and 500 6-particle clusters.

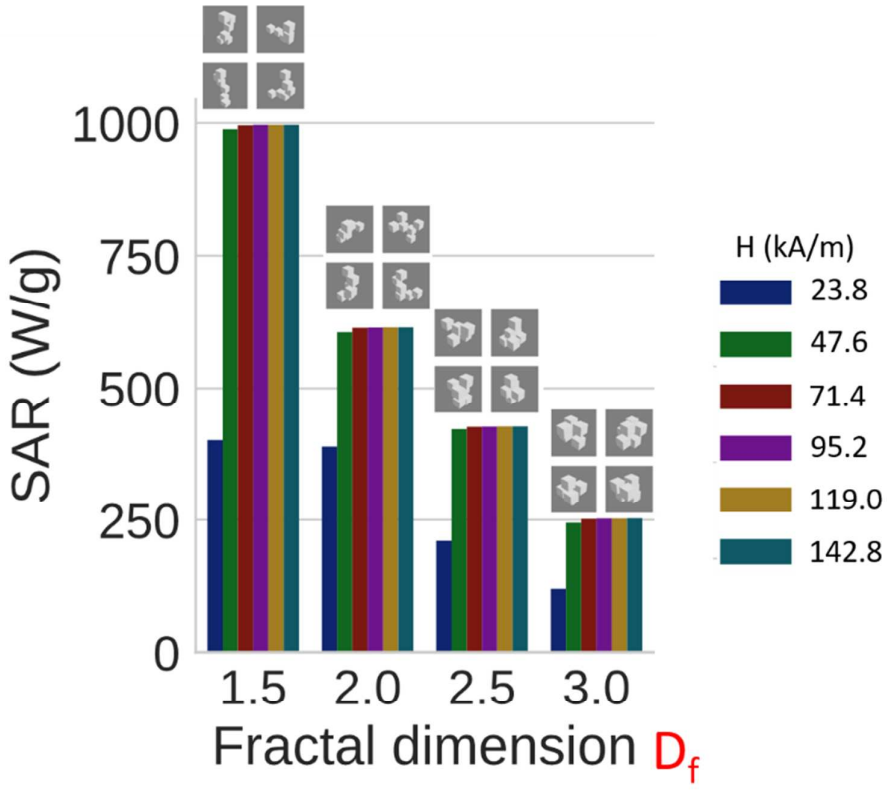

Figure S18: Calculated dependence of SAR on the fractal dimension D_f for ensembles of 6-particle clusters, for different applied fields. Note that fractal dimension D_f is a measure of asymmetry of the statistical arrangement of particles inside the clusters. As the D_f increases from 1 to 3 the statistical arrangement of particles inside the clusters changes from chain-like geometry (D_f ~ 1), through planar geometry (D_f ~ 2), to spherical geometry (D_f ~ 3). The values of SAR are the largest for statistically chain-like structures, and continually decrease with the increasing degree of geometrical symmetry. Spherical cluster geometries lead to the lowest values of SAR. Fractal dimension D_f = 3 applies to 6-particle clusters shown in Fig. 5 in the main text. Simulations assumed $K = 5 \times 10^4$ erg/cm^3, saturation magnetization $M_S =$ 450 emu/cm^3, and frequency $f = 300$ kHz. Ensembles of 6-particle clusters contained 3000 particles, *i.e.* 500 6-particle clusters.

References:

(1) Wetterskog, E.; Tai, C.; Grins, J.; Bergstrom, L.; Salazar-Alvarez, G. Anomalous Magnetic Properties of Nanoparticles Arising from Defect Structures: Topotaxial Oxidation of $Fe_{1-x}O/Fe_3O_4$ Core-Shell Nanocubes to Single-Phase Particles. *ACS Nano* **2013**, *7*, 7132–7144.

(2) Walter, A.; Billotey, C.; Garofalo, A.; Ulhaq-Bouillet, C.; Lefèvre, C.; Taleb, J.; Laurent, S.; Vander Elst, L.; Muller, R. N.; Lartigue, L.; Gazeau, F.; Felder-Flesch, D.; Begin-Colin, S. Mastering the Shape and Composition of Dendronized Iron Oxide Nanoparticles To Tailor Magnetic Resonance Imaging and Hyperthermia. *Chem. Mater.* **2014**, *26*, 5252–5264.

(3) Levy, M.; Quarta, A.; Espinosa, A.; Figuerola, A.; Wilhelm, C.; García-Hernandez, M.; Genovese, A.; Falqui, A.; Alloyeau, D.; Buonsanti, R.; Cozzoli, P. D.; García, M. A.; Gazeau, F.; Pellegrino, T. Correlating Magneto-Structural Properties to Hyperthermia Performance of Highly Monodisperse Iron Oxide Nanoparticles Prepared by a Seeded-Growth Route. *Chem. Mater.* **2011**, *23*, 4170–4180.